Journal of Energy Chemistry 116 (2026) 854–862

Contents lists available at ScienceDirect

Journal of Energy Chemistry

journal homepage: www.elsevier.com/locate/jechem

http://www.journals.elsevier.com/journal-of-energy-chemistry/

Hierarchically porous hollow architecture hosting dense Co/Fe single-atom sites for synergistic oxygen electrocatalysis

Le Wei [a,1], Xuetao Zhang [a,1], Zhanyong Xu [a], Xingyi Shu [a], Hongbo Lou [b], Fujun Lan [b,c], Songqi Gu [d], Ge Chen [a,*], Qiaoshi Zeng [b,c,*], Manling Sui [a], Xiaoxing Ke [a,*]

[a] College of Materials Science and Engineering, State Key Laboratory of Materials Low-Carbon Recycling, Beijing University of Technology, Beijing 100124, China
[b] Shanghai Key Laboratory of Material Frontiers Research in Extreme Environments (MFree), Shanghai Advanced Research in Physical Sciences (SHARPS), Shanghai 201203, China
[c] Center for High Pressure Science and Technology Advanced Research, Shanghai 201203, China
[d] Shanghai Synchrotron Radiation Facility, Shanghai Advanced Research Institute, Chinese Academy of Sciences, Shanghai 201204, China

ARTICLE INFO

Article history:
Received 22 November 2025
Revised 18 January 2026
Accepted 20 January 2026
Available online 2 February 2026

Keywords:
MOF-on-MOF
Single-atom catalysts
Bifunctional catalysts
3D electron tomography
Hierarchical hollow structure

ABSTRACT

Tailoring single-atom catalysts (SACs) is a never-ending topic for catalyst design, where support modification plays a pivotal role. The support is conventionally porous, targeted to host high-density single atoms and to allow effective mass transfer, particularly for electrochemical reactions. However, a suboptimal porous structure with low connectivity and closed pores, may negatively impact the electrochemical performance. Introducing cavity to hierarchical porous structures has recently emerged as a promising approach, but the synthesis often relies on etchants which are usually destructive, whereas the impact of hierarchical shell on electrocatalytic activity lacks detailed investigations. In this work, we propose a "MOF-on-MOF" strategyby constructing high-density Co/Fe dual single-atom catalysts with hierarchical porosity and hollow structure through one-step annealing. This approach simultaneously achieves active sites with dense Co/Fe sites and optimizes support architecture, enabling efficient reaction kinetics for oxygen reduction reactions (ORR)/oxygen evolution reactions (OER). The optimal Co_8Fe_2-N/C-900°C catalyst demonstrates outstanding bifunctional activity in alkaline media. Density functional theory (DFT) calculations reveal that the Co sites exhibit favorable adsorption of reaction intermediates, and the Fe sites boast a lower energy barrier, which is ensured by high-density Co/Fe dual atom sites through our approach. This work establishes a new route to SACs derived from ZIFs, offering a novel solution for the field.

1. Introduction

Single-atom catalysts (SACs) have attracted much attention during the past decades [1,2]. The design of single-atom sites from precise tailoring of supports and the maximized utilizations of active atomic species have led to applications of SACs in thermocatalysis [3], electrocatalysis [4,5], and energy storage [6,7], etc. Hence, optimizing SACs through support design, more importantly, achieving desired structures through synthesis, are the cornerstones of further applications. The synthesis approaches include wet-chemistry methods [8], atomic layer deposition [9], high-temperature atomic migration strategy [10], electrodeposition [11] and ZIFs-derivatives [12].

SACs derived from ZIFs have the advantages of high surface area, abundant active sites, and various combinations of non-noble-metals, due to customizable structures made of transition metals and tunable pore structures. Thereby, they have been widely used for electrocatalysis [13], and are mainly pyrolyzed through controlled annealing condition, precursor tuning, and post treatment. Wang et al. investigated the impact of annealing condition by *in situ* TEM, revealing the microstructural evolution of ZIF-67 during pyrolysis and thus proposing a general decomposition route for ZIFs [14]. Moreover, tuning the Zn^{2+}/Co^{2+} ratio in the precursor has been reported to tailor the porous structure and improve bifunctional activity [15]. To further optimize the porous structure, additional etching agents are commonly required. Waterhouse's group reported a NaCl-assisted two-step pyrolysis

* Corresponding authors.
E-mail addresses: chenge@bjut.edu.cn (G. Chen), zengqs@hpstar.ac.cn (Q. Zeng), kexiaoxing@bjut.edu.cn (X. Ke).
[1] These authors contributed equally to this work.

https://doi.org/10.1016/j.jechem.2026.01.044

method to synthesize Fe SACs with increased mesoporosity and enhanced PEMFC performance [16]. Subsequently, Tang et al. constructed ligand-defective ZIF-8@ZIF-67 featuring abundant mesoporous structures via acetic acid etching, enabling precise modulation of active-site density and graphitization degree [17].

Another aspect of SACs synthesis focuses on increasing active sites density through support design, where single atoms are not only tuned by coordinating N/C, but are also close enough to interact with each other. In the case of dual-single atoms, paired transition metals single atoms can optimize the adsorption/desorption energy, thereby boosting the electrocatalytic activity [18,19]. From this aspect, hollow structure emerges as a viable approach [20], where the formation of the shell support from a solid precursor substantially increases the density of transition metals. Additionally, the shell shortens mass transport distances, whereas both inner/outer surfaces are exposed, creating superior triple-phase reaction interfaces [21]. Therefore, combining hierarchical pores with hollow structures has become a current priority, with recent works demonstrated on NHZ-112/900 [22], Pt/h-Co-NC [23] and Fe/NS-C [24]. However, the synthesis approach either needs etching agent which deteriorates support structure [25], or involves multiple annealing steps which add on energy consumption and economic cost, making it unsuitable for scaling up [26,27].

In this work, we propose a "MOF-on-MOF" technique coupled with one-step annealing to synthesize SACs with hierarchical hollow supports, and demonstrate on Co-Fe dual-single-atom catalysts derived from ZIF-8, thereby adding a new pathway of synthesizing SACs to previous work synthesizing metal particles and compounds using the same approach [28–30]. By synthesizing ZIF@Co_8Fe_2 precursors with core–shell structures and annealing to remove ZIF core, hierarchically porous shell supporting Co-Fe dual single atoms is derived. The optimized Co_8Fe_2-N/C-900°C catalyst exhibits superior ORR and OER performance relative to commercial Pt/C and RuO_2, and is successfully demonstrated on zinc-air batteries (ZABs). Detailed characterizations using advanced electron microscopy reveal high densities of single atoms located on the shell, which optimize the adsorption/desorption energy as confirmed by DFT calculations. Additionally, we emphasize the support structure's importance through detailed characterizations and discussions. One-step annealing without etching agents avoids destruction to the support structure, and the hierarchical pores with both outer and inner sides exposed to reaction media accelerate mass transport.

2. Experimental

2.1. Synthesis of ZIF-8

4.927 g 2-MIM and 2.97 g $Zn(NO_3)_2{\cdot}6H_2O$ were separately dissolved in 50 mL methanol. The Zn^{2+} solution was then poured into the 2-MIM solution for magnetic stirring. The resulting mixture was stirred at room temperature and 400 r min^{-1} for 12 h, followed by static aging for an additional 12 h. Afterwards, the precipitates were collected through centrifugation, thoroughly washed with methanol several times. The products were then dried at 60°C overnight before properly stored.

2.2. Synthesis of ZIF@Co_8Fe_2

The as-synthesized ZIF-8 (150 mg) was dispersed in 50 mL methanol and ultrasonicated for 30 min. Subsequently, 0.4656 g $Co(NO_3)_2{\cdot}6H_2O$ and 0.1112 g $FeSO_4{\cdot}7H_2O$ were then added to the suspension for magnetic stirring. 20 mL methanol solution containing 0.656 g of 2-MIM was then poured into the suspension and continued stirring for 12 h. The resultant lilac powder was centrifugally washed with methanol three times and then dried at 60°C under vacuum overnight.

2.3. Synthesis of Co_8Fe_2-N/C

Carbonization of the above-synthesized ZIF@Co_8Fe_2 was carried out in Ar. The powder was separately heated to 800, 900 and 1000°C at a heating rate of 2°C min^{-1} and maintained for 1 h. The samples were designated as Co_8Fe_2-N/C-800°C, Co_8Fe_2-N/C-900°C and Co_8Fe_2-N/C-1000°C, respectively.

2.4. Others

Chemicals, synthesis of other samples, characterization methods, electrochemical tests, and theoretical calculations were detailed in the supporting information.

3. Results and discussion

3.1. The investigation of Co/Fe dual single atoms as active sites at atomic-scale

The synthesis of ZIF-8 derived target catalyst is illustrated in Fig. 1(a), with details provided in experimental section. Starting from ZIF-8 precursor, the surface was first coated by Co and Fe via solution approach, named as "ZIF@Co_8Fe_2" as shown in Fig. S1. Pyrolysis of the ZIF@Co_8Fe_2 was then performed at 800, 900 and 1000°C, respectively, yielding Co_8Fe_2-N/C-800°C, Co_8Fe_2-N/C-900°C and Co_8Fe_2-N/C-1000°C. The influence of annealing temperature on the samples' structures was first investigated. The XRD patterns of Co_8Fe_2-N/C-800°C and Co_8Fe_2-N/C-900°C display only two broad peaks at 25° and 44° (Fig. S2), corresponding to the (002) and (100) planes of graphitic carbon, suggesting the presence of defective carbon without long-range order [31]. Additionally, the Raman spectra (Fig. S3) reveal that the intensity ratio of the catalysts' D and G bands (I_D/I_G) decreases from 1.13 to 0.99 with increasing temperature, indicating enhanced graphitization and thus increased conductivity [32], as evidenced by EIS measurements (Fig. S4, Table S1).

The edges of Co_8Fe_2-N/C-800°C and Co_8Fe_2-N/C-900°C are enlarged in Fig. 1(b, c) as investigated by AC-STEM, clearly showing the distribution of single atoms. However, when the annealing temperature increases to 1000°C, nanoparticles precipitate (Fig. 1d). The EDS mapping confirms Co/Fe enrichment in the particles (Fig. S5), and the lattice spacing of 2.0 Å is consistent with the (1 1 0) crystal plane of f.c.c. Co-Fe alloy (Fig. 1d). In order to confirm the atomic species of single atoms in Co_8Fe_2-N/C-800°C and Co_8Fe_2-N/C-900°C, EDS spectra were collected on the samples, as shown in Fig. 1(e). The presence of C, N, Co, Fe, and Zn is confirmed, with corresponding quantification provided in Fig. S6. Since HAADF-STEM is a Z-contrast imaging technique, the atomic distribution at high magnifications in Fig. 1(b, c) can be confirmed to be Co/Fe and possibly Zn. Additionally, the nitrogen content was also examined since it influences the electrochemical performance through anchoring single atoms and tuning M-N_x active sites [33]. As shown by the quantification of the EDS spectra, the nitrogen content is found to be 9.9% in Co_8Fe_2-N/C-800°C, 7.4% in Co_8Fe_2-N/C-900°C, and decreases sharply to 2.6% in Co_8Fe_2-N/C-1000°C (Fig. S6 and Table S2). The loading of single atoms is critical to the performance of the catalysts. According to ICP-MS/OES analysis, the Co and Fe contents in Co_8Fe_2-N/C-900°C are 1.52 wt.% and 2.08 wt.% (Table S3), respectively, achieving a high-loading single-atom catalyst compared with methods reported in literature [13,34–36].

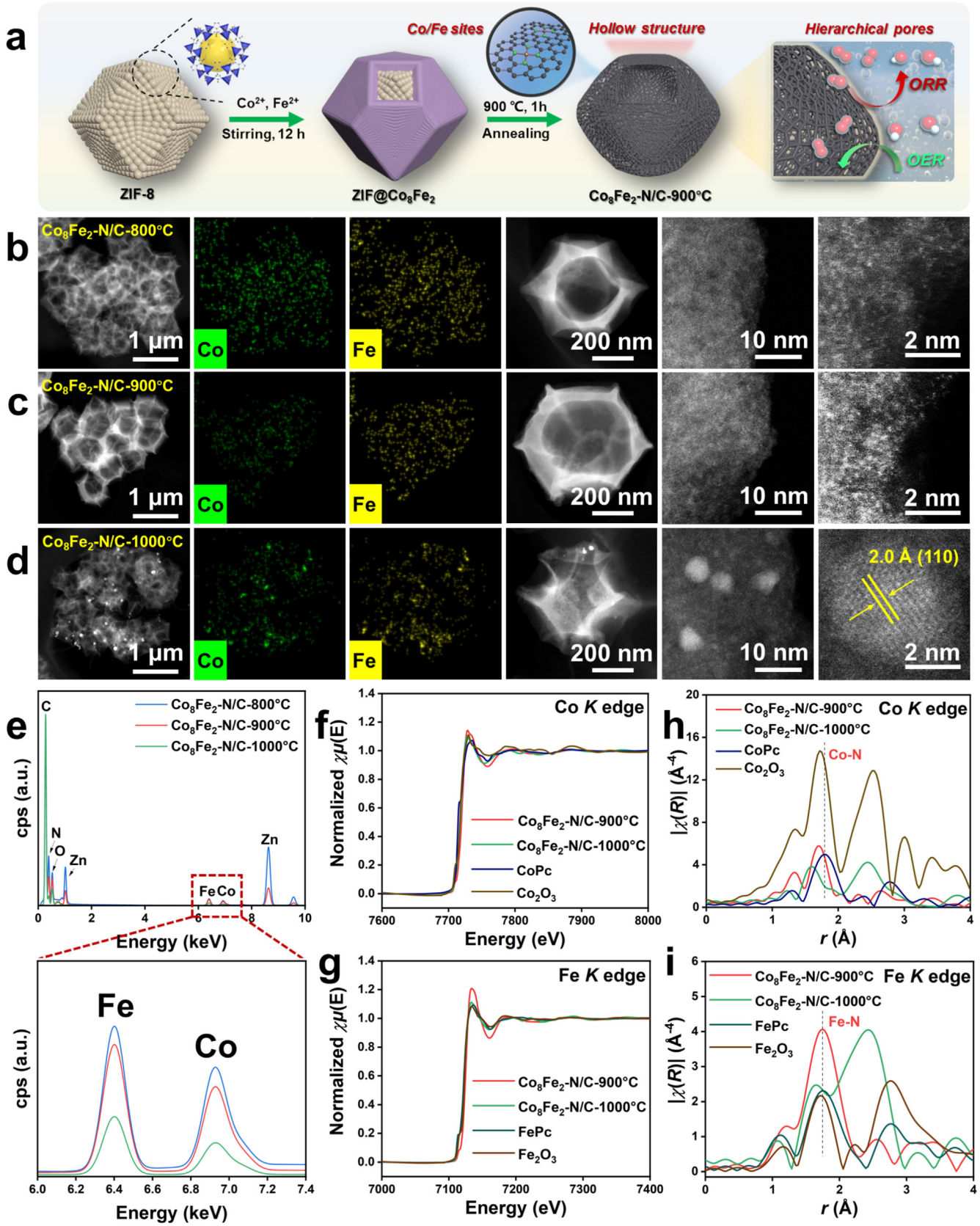

Fig. 1. Atomic-scale analysis of active sites. (a) Illustration of the synthesis of the Co_8Fe_2-N/C-900°C catalyst. (b–d) HAADF-STEM images and corresponding elemental mappings of Co and Fe, (e) EDS spectra of Co_8Fe_2-N/C-800°C, Co_8Fe_2-N/C-900°C and Co_8Fe_2-N/C-1000°C, respectively. K-edge XANES spectra of (f) Co and (g) Fe. K-edge Fourier-transformed EXAFS analysis in R space of (h) Co and (i) Fe.

To focus on the local electronic structure and coordinative environment of Co/Fe single atoms, X-ray absorption near edge structure (XANES) and extended X-ray absorption fine structure (EXAFS) analyses were conducted on the Co_8Fe_2-N/C-900°C and Co_8Fe_2-N/C-1000°C catalysts. The Co and Fe K-edge XANES spectra for Co_8Fe_2-N/C-900°C and Co_8Fe_2-N/C-1000°C resemble those of CoPc and FePc, respectively (Fig. 1f, g and Fig. S7), while the Co and Fe K-edge absorption energies for both Co_8Fe_2-N/C samples are slightly higher than that of CoPc and FePc, respectively. Hence it can be confirmed that the valence states of Co and Fe in the Co_8Fe_2-N/C samples are approximately between +2 and +4 [37]. Notably, both Co and Fe K-edge absorption energies in Co8Fe_2-N/C-900°C are slightly higher than in Co8Fe_2-N/C-1000°C, corresponding to the precipitation of zero-valent alloy at 1000°C.

The Fourier-transformed (FT) k^2-weighted EXAFS spectra of Co for Co_8Fe_2-N/C-900°C (Fig. 1h) shows the main peak at 1.71 Å, which is slightly smaller than the bond length of Co–N in CoPc (1.79 Å). Similarly, EXAFS spectra for Fe are shown in the Fig. 1 (i). A peak at 1.76 Å is identified in Co_8Fe_2-N/C-900°C, which overlaps with the Fe–N bond in FePc, suggesting that the Fe site is relatively more stable compared to the Co site. Meanwhile, both in Fig. 1(h, i), Co_8Fe_2-N/C-1000°C exhibits a bond length (2.43 Å) characteristic of Co-Fe alloy, consistent with the bond length in Co/Fe foil (Fig. S8). Furthermore, the wavelet transform (WT) contour map of Co_8Fe_2-N/C-900°C exhibited only Fe–N and Co–N coordination, demonstrating an atomically dispersed structure with metals bonded to N; meanwhile, M–M bonds were clearly observed in Co_8Fe_2-N/C-1000°C (Fig. S9). According to the EXAFS-fitting results, the coordination number of Co–N and Fe–N is about 4.4 and 3.8, respectively (Fig. S10 and Table S4), confirming that the Co/Fe atoms in Co_8Fe_2-N/C-900°C are atomically dispersed as Co-N_4 and Fe-N_4 configurations. Furthermore, the high-resolution N 1*s* XPS spectra of Co_8Fe_2-N/C series catalysts can be deconvoluted into five peaks, among which the M–N peak (399.8 eV) provides strong evidence for N coordination of the active sites. As the temperature increased, the metallic N content decreased from 18.3% to 8.1%, indicating that Fe–N and Co–N coordination was disrupted, which further led to the formation of alloy particles (Fig. S11). The results presented strongly indicate that the Co/Fe sites in Co_8Fe_2-N/C-900°C are atomically dispersed, offering a uniform and efficient catalytic center for both ORR and OER processes.

3.2. Electrochemical performance

The ORR and OER performance of as-synthesized catalysts were evaluated using a typical three-electrode system in an O_2-saturated 0.1 M KOH solution, and all potentials were referenced to the reversible hydrogen electrode (RHE), see details in Supplementary Information. As shown in Fig. 2(a), Co_8Fe_2-N/C-900°C exhibits a higher half-wave potential ($E_{1/2}$ = 0.894 V), compared to Co_8Fe_2-N/C-800°C ($E_{1/2}$ = 0.862 V), Co_8Fe_2-N/C-1000°C ($E_{1/2}$ = 0.854 V) and commercial Pt/C ($E_{1/2}$ = 0.861 V). The ORR kinetic behavior of Co_8Fe_2-N/C-900°C was further assessed by the Tafel plots (Fig. 2b). The Tafel slope for the Co_8Fe_2-N/C-900°C catalyst is 59.3 mV dec^{-1}, which is lower than those of commercial Pt/C (62.5 mV dec^{-1}), Co_8Fe_2-N/C-800°C (78.4 mV dec^{-1}) and Co_8Fe_2-N/C-1000°C (85.2 mV dec^{-1}), and is thus indicative of a more rapid ORR kinetics. The cycle stability of the aforementioned catalysts was examined through accelerated durability test (ADT). After 10,000 cycles, the Co_8Fe_2-N/C-900°C catalyst exhibits only a slight decline in its half-wave potential compared to commercial Pt/C (Fig. 2c and Fig. S12). Furthermore, using the Koutecky-Levich (K-L) equation and RRDE test, the electron transfer number for the Co_8Fe_2-N/C-900°C catalyst was calculated to be 3.72–3.76, with an H_2O_2 yield of approximately 10% (Fig. 2d and Fig. S13), confirming that the ORR process is dominated by the 4-electron pathway, accompanied by only a minor 2-electron side reaction.

Additionally, the Co_8Fe_2-N/C-900°C catalyst also demonstrated excellent oxygen evolution reaction (OER) activity in both 1 and 0.1 M KOH solutions. As shown in Fig. 2(e), the Co_8Fe_2-N/C-900°C electrode delivers a 310 mV overpotential at the current density of 10 mA cm^{-2} in 1 M KOH, outperforming RuO_2 (337 mV), Co_8Fe_2-N/C-800°C (341 mV) and Co_8Fe_2-N/C-1000°C (357 mV). With regard to its cycling stability, the overpotential shows a slight degradation to 347 mV after 3000 cycles at a scan rate of 0.2 V s^{-1}, which is close to or even lower than the initial performance of the samples for comparison (Fig. S14). Fig. 2(f) displays the OER performance of the Co_8Fe_2-N/C in 0.1 M KOH. The overpotential of the Co_8Fe_2-N/C-900°C is about 530 mV at the current density of 10 mA cm^{-2}, outperforming Co_8Fe_2-N/C-800°C (577 mV) and Co_8Fe_2-N/C-1000°C (626 mV). After 3000 cycles, the overpotential of Co_8Fe_2-N/C-900°C degrades to 582 mV, which is still lower than that of Co_8Fe_2-N/C-800°C (622 mV) and Co_8Fe_2-N/C-1000°C (649 mV) (Fig. S15).

To investigate the influence of single-atom density on catalytic performance, x0.5-Co_8Fe_2-N/C-900°C and x1.5-Co_8Fe_2-N/C-900°C were synthesized (Fig. S16a, b). In x0.5-Co_8Fe_2-N/C-900°C, the Co/Fe sites remained as single atoms, whereas Co-Fe alloy and CoC_x phases emerged in x1.5-Co_8Fe_2-N/C-900°C (Fig. S16c). The Co and Fe contents in the catalysts increased accordingly with the feed amount (Fig. S16d, e). With regard to ORR/OER performance, Co_8Fe_2-N/C-900°C also exhibited superior catalytic activity and stability compared to x0.5-Co_8Fe_2-N/C-900°C ($E_{1/2}$ = 0.858 V, $E_{j=10}$ = 385 mV) and x1.5-Co_8Fe_2-N/C-900°C ($E_{1/2}$ = 0.834 V, $E_{j=10}$ = 361 mV) (Fig. S17). It is hence clear that insufficient active site loading in x0.5-Co_8Fe_2-N/C-900°C and non-uniform metal particle precipitation in overloaded x1.5-Co_8Fe_2-N/C-900°C resulted in inferior performance. Meanwhile, to demonstrate the impact of hierarchical pores on catalytic performance, a hollow Co/Fe dual single-atom catalyst with only micropores was synthesized (Figs. S18 and S19) [38]. Despite its high specific surface area of 985.6 m^2 g^{-1}, microporous-CoFe-N/C exhibits inferior ORR/OER activity ($E_{1/2}$ = 0.836 V, $E_{j=10}$ = 355 mV) and limiting current density compared to Co_8Fe_2-N/C-900°C, manifesting the critical role of hierarchical porous structures (Fig. S20).

In summary, Co_8Fe_2-N/C-900°C demonstrates a superior ORR half-wave potential and a lower OER overpotential before and after cycle, which indicates its excellent bifunctional electrochemical activity (Fig. 2g). To further quantify the bifunctional catalytic activity of Co_8Fe_2-N/C catalyst, the potential difference ΔE between $E_{1/2}$ for ORR and $E_{j=10}$ for OER was evaluated (Fig. 2h), where a smaller value of ΔE (calculated as $\Delta E = E_{j=10} - E_{1/2}$) indicates higher activity. Co_8Fe_2-N/C-900°C shows the lowest ΔE of 0.86 V, compared to Co_8Fe_2-N/C-800°C (0.95 V) and Co_8Fe_2-N/C-1000°C (1.02 V). This phenomenon can be attributed to the low electrical conductivity of Co_8Fe_2-N/C-800°C, while the precipitation of alloy particles in Co_8Fe_2-N/C-1000°C leads to decreased activity.

Co_8Fe_2-N/C-900°C catalysts were further set up for potential applications as air electrodes for ZABs, as schematically illustrated in Fig. 3(a). Details can be found in Supplementary Information. As shown in Fig. 3(b), ZABs using Co_8Fe_2-N/C-900°C as cathode provide an open circuit potential (OCP) of 1.432 V, outperforming that of Pt/C (1.368 V). The higher open-circuit potential of the Co_8Fe_2-N/C-900°C catalyst indicates its superior catalytic activity, thereby contributing to enhanced energy output under operating conditions. The discharge/charge polarization curve reveals that the ZABs utilizing Co_8Fe_2-N/C-900°C exhibit an overpotential of merely 0.49 V at a current density of 10 mA cm^{-2}, notably lower than that of Pt/C cathode (0.89 V) (Fig. 3c), and thus indicates an accelerated kinetic process. The rate performance of the ZABs was further examined at various current densities. As presented in Fig. 3(d),

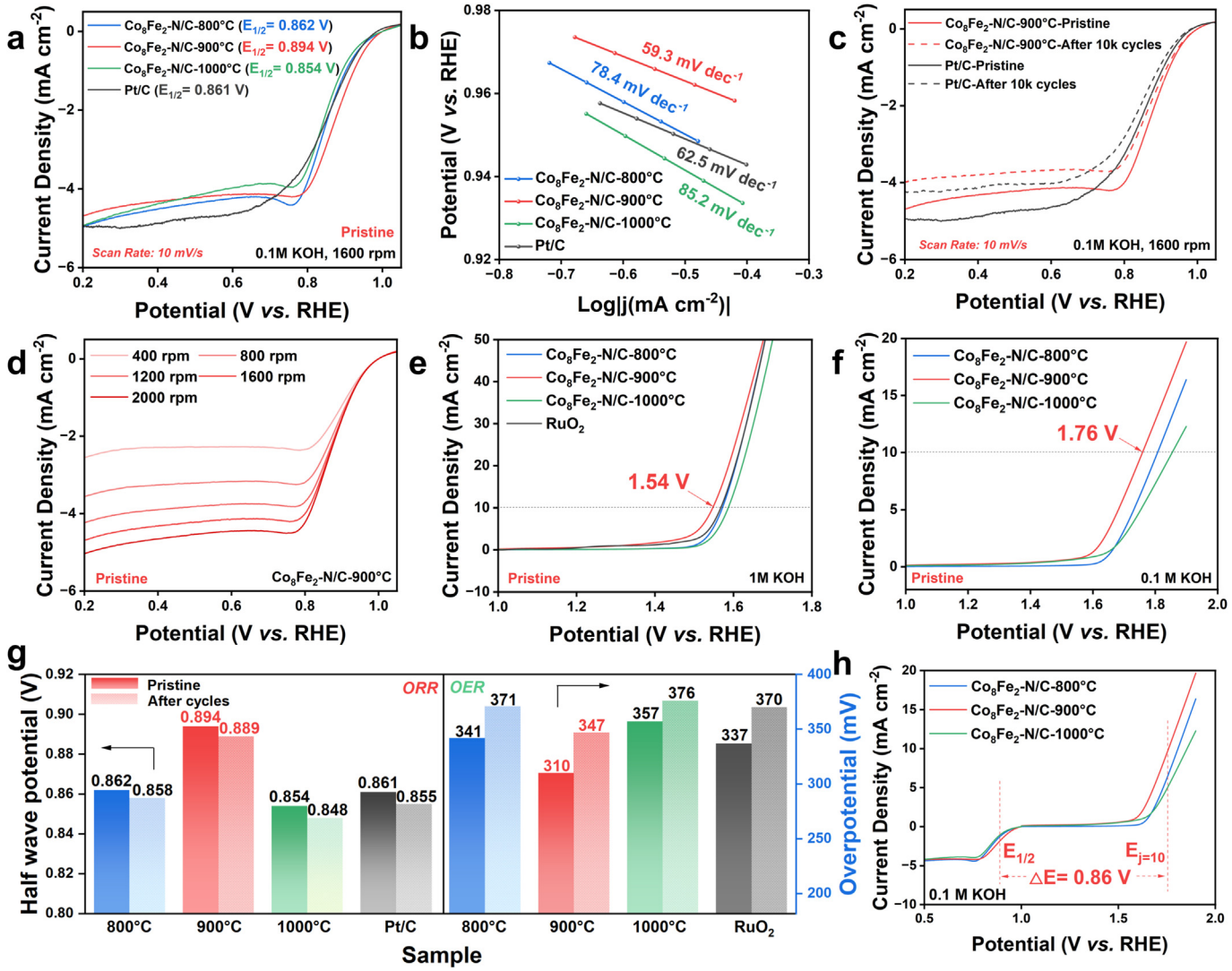

Fig. 2. Electrochemical performance of Co_8Fe_2-N/C. (a) ORR LSV curves of Co_8Fe_2-N/C-800°C, Co_8Fe_2-N/C-900°C, Co_8Fe_2-N/C-1000°C and Pt/C at a rotating rate of 1600 r min^{-1}. (b) Associated Tafel plots derived from the ORR LSV curves. (c) ORR LSV curves of Co_8Fe_2-N/C-900°C and Pt/C before and after 10,000 cycles. (d) ORR LSV curves of Co_8Fe_2-N/C-900°C at different rotating rates. (e) OER LSV curves of Co_8Fe_2-N/C-800°C, Co_8Fe_2-N/C-900°C, Co_8Fe_2-N/C-1000°C and RuO_2 in 1 M KOH. (f) OER LSV curves of Co_8Fe_2-N/C-800°C, Co_8Fe_2-N/C-900°C and Co_8Fe_2-N/C-1000°C in 0.1 M KOH. (g) Summary of ORR/OER catalytic performance of the above catalysts before and after cycles. (h) LSV curves of Co_8Fe_2-N/C-800°C, Co_8Fe_2-N/C-900°C and Co_8Fe_2-N/C-1000°C catalysts across the full OER/ORR region in 0.1 M KOH.

the ZABs with Co_8Fe_2-N/C-900°C cathode exhibit a higher discharge plateau compared to Pt/C, regardless of the current density applied. Notably, after enduring high current density discharge of 50 mA cm^{-2} and reverting to 1 mA cm^{-2}, the discharge plateau remains unchanged compared to initial measurement. The ZAB also operated stably for 450 cycles at a current density of 5 mA cm^{-2} (Fig. S21), demonstrating its superior catalytic activity and stability. Moreover, when tested at current density of 10 mA cm^{-2}, the specific capacities normalized to the consumed Zn mass for the Co_8Fe_2-N/C-900°C and Pt/C catalysts are 815.7 and 736.4 mA h g_{Zn}^{-1}, respectively (Fig. 3e). The maximum power density is measured to be 241.1 and 144.0 mW cm^{-2} for Co_8Fe_2-N/C-900°C and Pt/C, respectively (Fig. 3f). Furthermore, in order to reveal the advantages of our optimized catalysts in enhanced ZAB performance, H-Fe-N/C and H-Co-N/C (Fig. S22a, b) and CoFe-N/C (Fig. S23a) were synthesized, and the atomic dispersion of active sites in the as-synthesized catalysts are confirmed (Figs. S22c–e and S23b–d). At the same catalyst loading and electrode fabrication, Co_8Fe_2-N/C-900°C exhibits lower overpotential but higher OCP, maximum power density and specific capacity compared to mixed H-Fe-N/C/H-Co-N/C and CoFe-N/C, demonstrating superior rate performance (Fig. S24). This again confirms that both the synergistic effect between Co and Fe sites and the presence of the hollow structure are crucial for enhancing device performance. Finally, we compared the performance of our device with that reported in literature, and summarized the power density, specific capacity, and discharge/charge overpotential in Fig. 3(g, h). ZABs using Co_8Fe_2-N/C-900°C as cathode surpass commercial Pt/C electrode and most Co/Fe single-atom catalysts reported in literature (Table S5) [39–53].

3.3. Boosted performance by unique structure design

In order to understand the performance enhancement of our ZIF-derived Co/Fe bimetallic single-atom catalyst, we first calculated the Gibbs free energy changes (ΔG) by density functional theory (DFT), where the corresponding thermodynamic processes of OER and ORR are schematically shown in Fig. 4(a).

According to previous results (Fig. S13), the ORR process goes through a $4e^-$ pathway in an alkaline environment. As illustrated

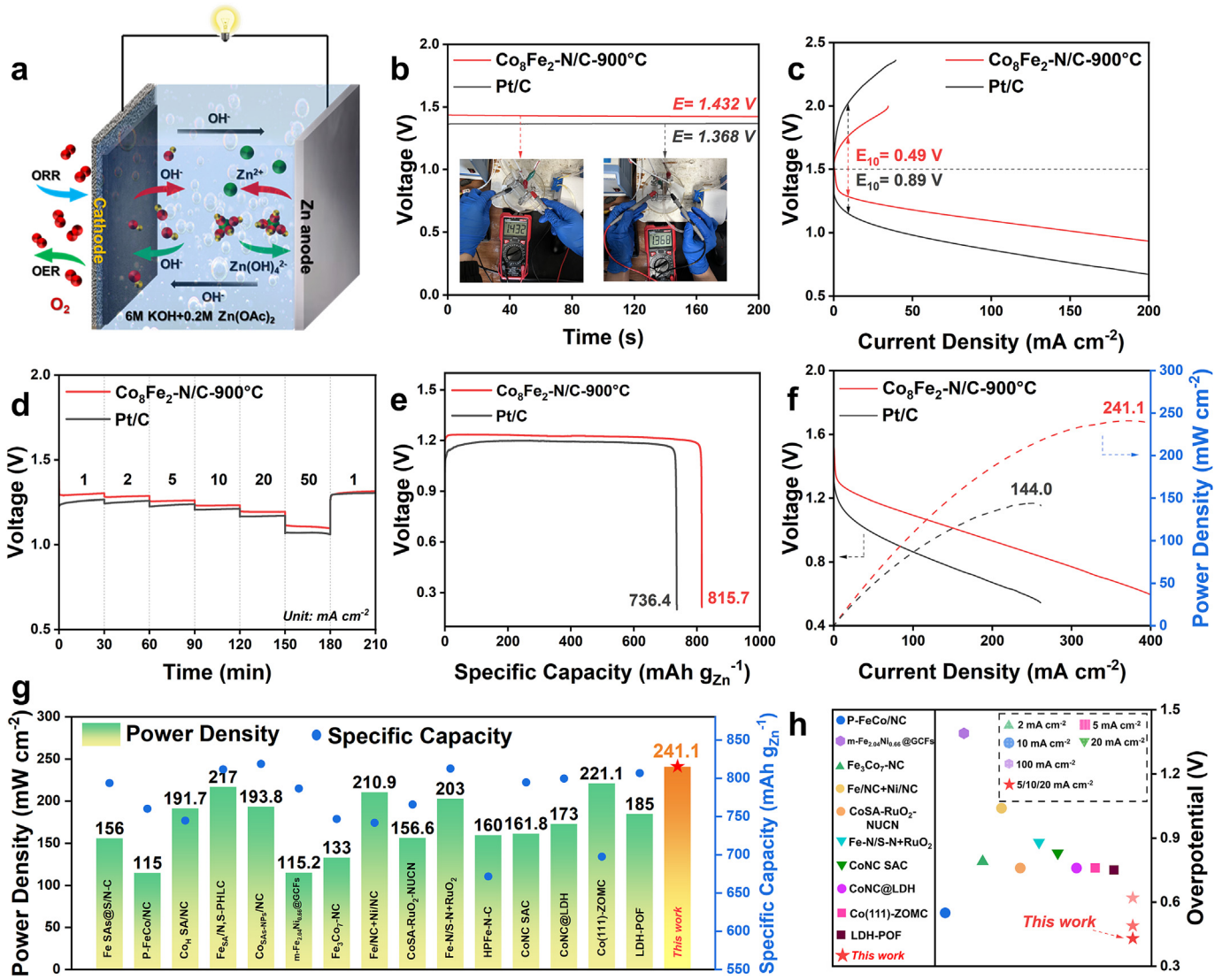

Fig. 3. Electrochemical performance of assembled zinc-air battery. (a) Schematic diagram of the liquid ZABs configuration. (b) Open circuit potential plot with the inset showing a stable OCP. (c) Discharge/charge polarization curves, (d) rate performance, (e) specific capacity curves of ZABs normalized with the Zn consumed, and (f) polarization and power density plots using Co_8Fe_2-N/C-900°C and Pt/C as catalysts. (g, h) Comparison of power density, specific capacities, and overpotential from this work with Co/Fe single-atom catalysts reported in literature [39–53].

by red arrows in Fig. 4(a), this process begins with the adsorption of O_2 from the electrolyte, leading to the formation of the peroxide intermediate (OOH*). Subsequently, this intermediate gains electron to form O* and OH* species, and the OH* intermediate is further reduced to produce OH^- (OER process is reversed as indicated by green arrows). All four conditions were calculated, i.e., Co-site of Co/Fe dual-single-atoms (abbreviated as (CoFe)–Co site), Fe-site of Co/Fe dual-single-atoms (abbreviated as (CoFe)-Fe site), Co-single-atom and Fe-single-atom. As shown in Fig. 4(b) and Tables S6–S10, when converting O_2 to OOH* at the equilibrium potential (U = 1.23 V vs. RHE), compared to other site configurations, (CoFe)-Fe site exhibits a reaction free energy less than 0 eV, which means the reaction at this site is spontaneous and more efficient. The result thus indicates that the presence of Co effectively modulates the electronic environment around the Fe sites, thereby reducing the reaction energy barriers and enhancing catalytic activity. Unexpectedly, while the (CoFe)–Co site requires the lowest energy for the non-spontaneous OH*→OH^- step (0.198 eV), in the specific step of O_2 conversion to OOH*, ΔG for the (CoFe)–Co site (0.396 eV) is slightly higher than that of the Co-site (0.256 eV). In summary, the Co-Fe bimetallic site demonstrates overall advantages compared to single metal sites in catalyzing both ORR and OER. The (CoFe)-Fe sites spontaneously promote the O_2→OOH* conversion, whereas (CoFe)–Co sites require the lowest energy for the OH*→OH^- transformation, despite sacrificing part of their inherent catalytic activity in the specific step. This phenomenon also reveals that the synergistic effect between Co/Fe dual single-atom sites doesn't involve simultaneous enhancement of catalytic activity, but rather optimizes the reaction pathway.

We further investigated the optimization of electronic structure introduced by co-presence of Co and Fe sites. Charge density difference analysis shows that Fe-N_4 sites possess strong localized charge polarization, effectively modulating adsorbate electronic structures to enhance reactivity, whereas Co-N_4 sites show a more uniform charge distribution (Fig. S25). This electronic structure difference induces charge redistribution, optimizing the adsorption and activation of reaction intermediates. For both sites, electronic states near the Fermi level are dominated by transition metal *d*-orbitals, indicating that metal center reactivity during the ORR

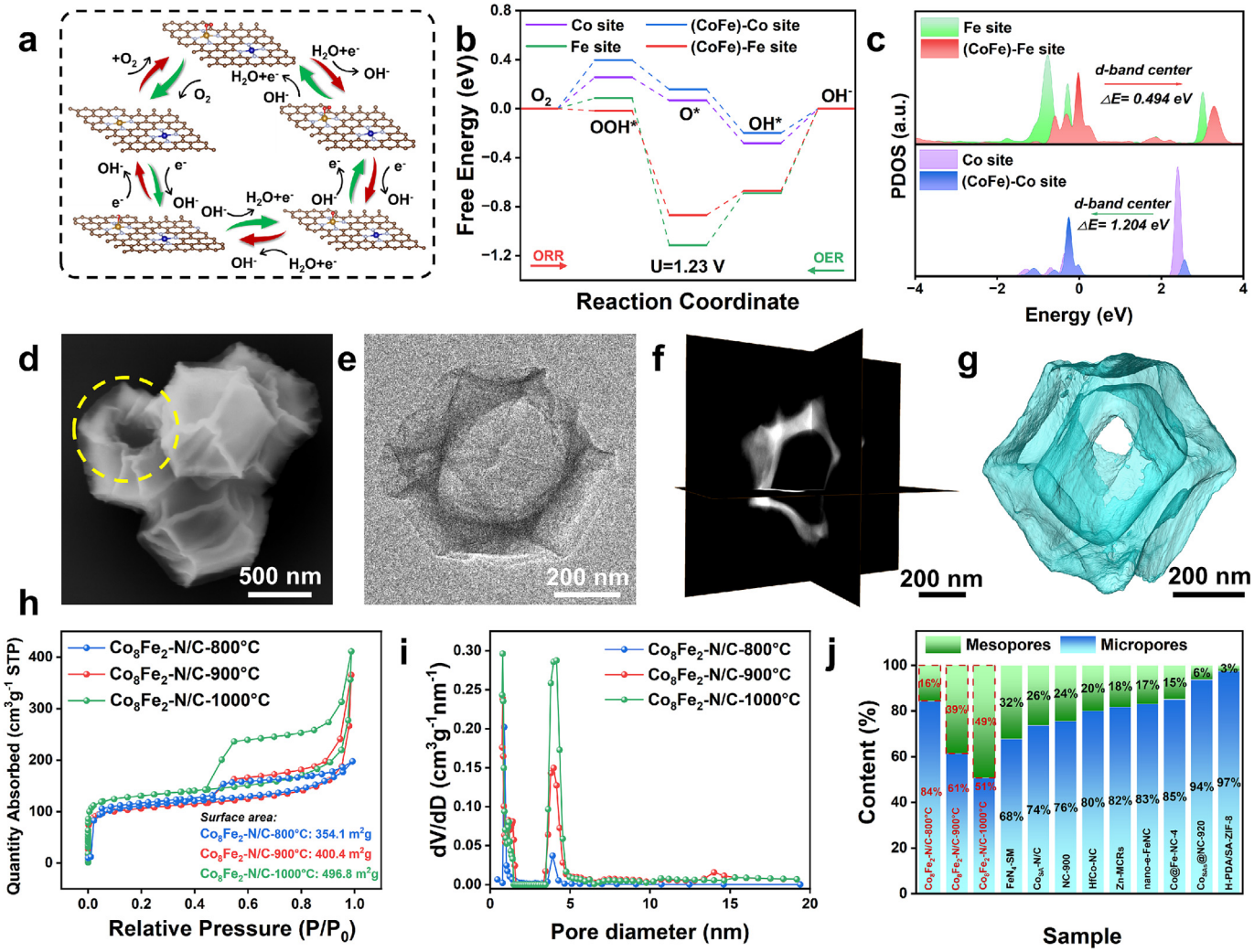

Fig. 4. Coordination environment, reaction mechanism and structural analysis of Co_8Fe_2-N/C. (a) Schematic diagram of electrochemical process reaction (red arrow corresponds to ORR, green arrow corresponds to OER). (b) Reaction energy change and (c) DOS of Co site, Fe site, (CoFe)–Co site and (CoFe)-Fe under U = 1.23 V. (d) SEM and (e) TEM images of Co_8Fe_2-N/C-900°C. (f) Cross-sectional view of Co_8Fe_2-N/C-900°C reconstructed from 3D electron tomography and shown in xy, xz and yz planes. (g) 3D reconstruction of Co_8Fe_2-N/C-900°C showing its cavity. (h, i) N_2 adsorption–desorption isotherms and pore-size distribution curve of Co_8Fe_2-N/C-800°C, Co_8Fe_2-N/C-900°C and Co_8Fe_2-N/C-1000°C. (j) Comparison of mesopore and micropore ratios between Co_8Fe_2-N/C and previously reported catalysts in the literature [36,55–62].

process is mainly governed by the *d*-orbital electronic structure (Fig. S26a). In the presence of Fe sites, the *d*-band center of Co significantly shifts from 0.678 to –0.526 eV, indicating the binding strength between Co sites and reaction intermediates is weakened, thereby optimizing the adsorption of reaction intermediates (Fig. 4c and Fig. S26b). At the same time, the *d*-band center of Fe in the presence of Co shows a positive shift from –0.741 to –0.247 eV. Since it is closer to the Fermi level, electrons are easier to transfer from the catalyst surface to the reaction intermediates [54]. In summary, the overall electronic structure of the Co/Fe dual single-atom catalyst is enhanced, where the Co site is more favorable for the adsorption of reaction intermediates and the Fe site better facilitates the conversion of catalytic reactants.

Back to fundamentals of electrochemical performance, the reaction is not solely dependent on the active sites, whereas the support structure is equally crucial by enhancing mass transfer. Hence the microstructure of Co_8Fe_2-N/C was examined in detail in Fig. 4(d, e). To reveal the internal structure of catalysts, the samples are pulverized by ultrasonic cell disruptor and studied by scanning electron microscopy (SEM) as shown in Fig. 4(d). The catalyst retains dodecahedral structure with surface wrinkles, attributed to the inward depression of the surface and convex edges. The yellow circle highlights cavity at a damaged corner of the supports. TEM image of Fig. 4(e) confirms the cavity by a lighter contrast in the center compared to the edges. The internal structure was further analyzed by 3D electron tomography. Fig. 4(f) displays the cross-section view of Co_8Fe_2-N/C-900°C in *xy*, *yz* and *xz* planes (see Video S1) and Fig. 4(g) presents the reconstruction in 3D, clearing reveal the inner hollow structure.

N_2 adsorption–desorption curves (Fig. 4h) demonstrate that all three samples exhibit type IV isotherms, which are characterized by rapid growth at low relative pressures ($P/P_0 < 0.05$) and a unique hysteresis loop at high relative pressures ($P/P_0 > 0.4$), indicative of abundant mesopores and micropores. The Brunauer-Emmett-Teller (BET) specific surface areas for Co_8Fe_2-N/C-800°C, Co_8Fe_2-N/C-900°C and Co_8Fe_2-N/C-1000°C are measured as 354.1, 400.4, and 496.8 $m^2\ g^{-1}$, respectively. Furthermore, the pore size distributions (Fig. 4i) reveal that the samples annealed at different temperatures all have dominant peaks corresponding to micropores (<2 nm) and mesopores (2–5 nm), respectively. Notably, the relative intensity of mesopore peak increases with rising temperature, raising the mesopore proportion from 16% to 49%, demonstrating the formation of abundant hierarchical porous structures during pyrolysis. A chart is presented to compare the micropore

to mesopore ratio of our samples to those reported in literature [36,55–62], clearly demonstrating the enrichment of mesopores in our catalyst (Fig. 4j).

To elucidate the formation mechanism of the hollow structure and hierarchical pores in ZIF@Co_8Fe_2 during annealing, temperature-ramping experiments were performed from 300 to 700°C based on thermogravimetric analysis (TGA) (Fig. S27a). XRD patterns show that a weak signal corresponding to CoFe alloy appeared at 44.8° under 500°C, which gradually intensified as the temperature increased to 700°C (Fig. S27b). Additionally, peaks at 41.3° and 47.9° corresponding to the ZnO phase were observed at 600°C, indicating the initiation of Zn evaporation and the signal disappeared at 700°C, implying the ZnO decomposition. Based on the aforementioned characterization results, when the temperature was increased to 800°C and 900°C and maintained for 1 h, the CoFe alloy particles gradually disappeared, leaving a hierarchical porous structure and Co/Fe dual single-atom sites [63,64]. Subsequently, samples at different temperatures were characterized by STEM and EDS mapping (Fig. S27c–h). As the temperature gradually increased to 500°C, the support structure remained intact and alloy particles precipitated (Fig. S28). At 600°C, localized hollow structures appeared inside the support, and ZnO was observed on its surface (Fig. S29), indicating that the formation of the hollow structure is associated with Zn evaporation. As the temperature increased, Zn species further volatilized, ultimately leading to the formation of a complete hollow structure within the support. Thus, the formation and dispersion of CoFe alloy particles and the evaporation of Zn species during the annealing process are responsible for the formation of hierarchical pores and hollow structures in Co_8Fe_2-N/C-900°C without the need for additional etchants.

Moreover, structural characterization was conducted on the catalyst after 3000 OER cycles. Despite being partially etched, the post-cycled Co_8Fe_2-N/C-900°C maintained its initial dodecahedral structure (Fig. S30). At the same time, the XPS spectra of the initial and cycled samples of Co_8Fe_2-N/C-900°C were compared (Fig. S31). The O 1*s* spectrum indicates that the increase in C–O (533.2 eV) is attributed to gradual carbon surface oxidation under the strong OER environment, where original C=O (532.0 eV) groups may be further oxidized or undergo bond cleavage to form more stable C–O species (Fig. S31b). Besides, Fe^0 (706.7 and 719.5 eV) and Co^0 (778.2 and 793.4 eV) signals remained undetectable after cycle (Fig. S31c, d), confirming the stability of single-atom sites during the electrochemical process, while performance degradation after OER cycle is primarily attributed to carbon support damage.

To summarize, the featured microstructure of our catalyst further boosts the electrochemical performance from two aspects. Firstly, the "MOF-on-MOF" strategy followed by one-step annealing results in an open-structure with cavity, which not only increases the exposed surface area, but also increase the density of Fe/Co sites by maximizing the use of precursor. Secondly, this unique strategy generates a hierarchical porous structure enriched with mesopores, which significantly facilitates the mass transport. This approach demonstrates the advantages of energy-saving by one-step annealing and achieves an ideal structure without introducing additional pore-forming agents.

4. Conclusions

In summary, the Co_8Fe_2-N/C-900°C catalyst was designed and synthesized in this work via a "MOF-on-MOF" strategy. It exhibited a high ORR half-wave potential of 0.894 V and a low overpotential of 310 mV for the OER process at a current density of 10 mA cm^{-2}, which indicates its excellent bifunctional electrocatalytic activity. When used as ZAB cathodes, Co_8Fe_2-N/C-900°C demonstrate lower overpotential of 0.49 V at a current density of 10 mA cm^{-2}, a higher specific capacity of 815.7 mA h g_{Zn}^{-1}, and a high power density of 241.1 mW cm^{-2}, which outperforms most Co/Fe single-atom catalysts reported in literature. DFT calculations show that the presence of Co effectively modulates the electronic structure surrounding the Fe sites, thereby reducing the reaction energy barriers and enhancing catalytic activity. Moreover, this method utilizes the evaporation of Zn and the precipitation/dispersion of CoFe alloy to simultaneously constructs hierarchically porous hollow structures, while introducing bimetallic active sites, without requiring additional etching agents. This approach significantly accelerates mass transport dynamics, while maximizing exposure of reactive active sites, thus substantially improving the electrochemical performance of Co_8Fe_2-N/C-900°C. It reduces process complexity and offers valuable insights for designing support structures in high-performance catalyst systems.

CRediT authorship contribution statement

Le Wei: Writing – original draft. **Xuetao Zhang:** Data curation. **Zhanyong Xu:** Data curation. **Xingyi Shu:** Data curation. **Hongbo Lou:** Data curation. **Fujun Lan:** Data curation. **Songqi Gu:** Data curation. **Ge Chen:** Supervision. **Qiaoshi Zeng:** Supervision. **Manling Sui:** Supervision. **Xiaoxing Ke:** Supervision.

Declaration of competing interest

The authors declare that they have no known competing financial interests or personal relationships that could have appeared to influence the work reported in this paper.

Acknowledgement

L. Wei and X. Ke acknowledge the National Natural Science Foundation of China, China (12274010, 12474003). X. Ke and G. Chen acknowledge the Beijing Nova Program, China (20240484584). Q. Zeng acknowledges the support from the Shanghai Key Laboratory of Material Frontiers Research in Extreme Environments, China (22dz2260800), the Shanghai Science and Technology Committee, China (22JC1410300), and the Shanghai Synchrotron Radiation Facility of BL14W1 (https://cstr.cn/31124.02.SSRF.BL14W1). The authors thank Dr. Dazhe Xu and Yuxin Liu from HPSTAR for their assistance with the XAS experiments.

Appendix A. Supplementary material

Supplementary data to this article can be found online at https://doi.org/10.1016/j.jechem.2026.01.044.

References

[1] M. Urso, X. Ju, R. Nittoor-Veedu, H. Lee, D. Zaoralová, M. Otyepka, M. Pumera, ACS Catal. 15 (2025) 11617–11663.
[2] A. Wang, J. Li, T. Zhang, Nat. Rev. Chem. 2 (2018) 65–81.
[3] Y. Ren, C. Zhang, H. Wang, J.X. Liang, C. Zhu, H.S. Hu, J. Li, Chin. J. Struct. Chem. 44 (2025) 100649.
[4] Y. Li, H. Jiang, L. Lin, Z. Sun, G. Sun, J. Energy Chem. 102 (2025) 413–420.
[5] Y. Qi, Q. Liang, K. Song, X. Zhou, M. Liu, W. Li, F. Liu, Z. Jiang, X. Zou, Z. Chen, W. Zhang, W. Zheng, J. Energy Chem. 95 (2024) 306–314.
[6] S. Chen, G. Li, Z. Zhu, R. Zhu, J. Zhang, Y. Yue, G. Li, L. Zhou, Z. Yan, J. Energy Chem. 107 (2025) 440–458.
[7] J. Xu, Q. Kang, B. Peng, Z. Zhuang, D. Wang, L. Ma, J. Energy Chem. 106 (2025) 768–790.
[8] X. Guo, M. Yang, J. Hou, H. Li, Z. Liu, Y. Cui, D. Shi, H. Hu, B. Zhang, Y. Shao, Y. Wu, X. Hao, Chem. Eng. J. 513 (2025) 162955.
[9] J. Zhang, Z. Song, X. Yao, Y. Guan, Z. Huo, N. Chen, L. Zhang, X. Sun, Chem 11 (2025) 102498.
[10] Y. Qu, Z. Li, W. Chen, Y. Lin, T. Yuan, Z. Yang, C. Zhao, J. Wang, C. Zhao, X. Wang, F. Zhou, Z. Zhuang, Y. Wu, Y. Li, Nat. Catal. 1 (2018) 781–786.
[11] Z. Zhang, C. Feng, C. Liu, M. Zuo, L. Qin, X. Yan, Y. Xing, H. Li, R. Si, S. Zhou, J. Zeng, Nat. Commun. 11 (2020) 1215.

[12] M. Qi, M.J. Zachman, Y. Li, Y. Zeng, S. Hwang, J. Liang, M. Lyons, Q. Zhao, Y. Mao, Y. Shao, Z. Feng, Z. Wang, Y. Zhao, G. Wu, Energy Environ. Sci. 18 (2025) 5643–5656.
[13] M. Sun, S. Xi, S. Zhu, Y. Zhou, C. Li, B. Meng, J. Wei, X. Chi, X. Yu, Y. Cao, Y. Huang, X. Liu, J. Wang, Adv. Funct. Mater. (2025) e17645. https://doi.org/10.1002/adfm.202517645.
[14] Z. Wang, X. Ke, K. Zhou, X. Xu, Y. Jin, H. Wang, M. Sui, J. Mater. Chem. A 9 (2021) 18515–18525.
[15] G. Wang, M. Zhang, G. Zhang, Z. Wang, X. Chen, X. Ke, C. Wang, S. Chu, M. Sui, Adv. Funct. Mater. 34 (2023) 2308876.
[16] Q. Wang, Y. Yang, F. Sun, G. Chen, J. Wang, L. Peng, W.T. Chen, L. Shang, J. Zhao, D. Sun-Waterhouse, T. Zhang, G.I.N. Waterhouse, Adv. Energy Mater. 11 (2021) 2100219.
[17] Y. Tang, J. Ruan, Y. Xin, X. Ren, H. Yuan, X. Liu, Q. Chen, Chem. Eng. J. 511 (2025) 161999.
[18] T. Zhang, Y. Liu, L. Xue, J. Sun, P. Xiong, J. Zhu, J. Energy Chem. 94 (2024) 273–287.
[19] X. Hu, Z. Wu, C. Xu, J. Energy Chem. 97 (2024) 520–528.
[20] J. Wu, Y. Zhu, A. Cai, X. Fan, W. Peng, Y. Li, J. Energy Chem. 98 (2024) 634–644.
[21] G. Prieto, H. Tüysüz, N. Duyckaerts, J. Knossalla, G.H. Wang, F. Schüth, Chem. Rev. 116 (2016) 14056–14119.
[22] A. Panda, A. Sebastian, R. Nandan, J. Henzie, O. Cretu, J. Xu, N. Velychkivska, R. Ma, K. Kimoto, Y. Asakura, K. Iwase, L.K. Shrestha, K. Ariga, Y. Yamauchi, J.P. Hill, Chem. Eng. J. 516 (2025) 163959.
[23] Y. Lee, J.H. Lee, D. Lee, S. Oh, J. Park, K. Im, S.J. Yoo, J. Kim, Chem. Eng. J. 500 (2024) 157072.
[24] L. Cui, J. Hao, Y. Zhang, X. Kang, J. Zhang, X.Z. Fu, J.L. Luo, J. Colloid Interf. Sci. 650 (2023) 603–612.
[25] S. Wang, L. Luo, A. Wu, D. Wang, L. Wang, Y. Jiao, C. Tian, Coordin. Chem. Rev. 498 (2024) 215464.
[26] S. Das, J.M.H. Anal, P. Kalita, L. Saikia, S.L. Rokhum, P. Bhuyar, Int. J. Energy Res. 2023 (2023) 6676844.
[27] X. Jin, J. Lu, J. Li, Y. Zhou, J. Cleaner Prod. 471 (2024) 143392.
[28] K. Li, Y. Zhang, P. Wang, X. Long, L. Zheng, G. Liu, X. He, J. Qiu, J. Alloys Compd. 903 (2022) 163701.
[29] H. Zhang, A. Chen, Z. Bi, X. Wang, X. Liu, Q. Kong, W. Zhang, L. Mai, G. Hu, ACS Nano 17 (2023) 24070–24079.
[30] Y. Zou, Y. Yan, Q. Xue, C. Zhang, T. Bao, X. Zhang, L. Yuan, S. Qiao, L. Song, J. Zou, C. Yu, C. Liu, Angew. Chem. Int. Ed. 63 (2024) e202409799.
[31] X. Zhou, Z. Jia, A. Feng, X. Wang, J. Liu, M. Zhang, H. Cao, G. Wu, Carbon 152 (2019) 827–836.
[32] A.A.K. King, B.R. Davies, N. Noorbehesht, P. Newman, T.L. Church, A.T. Harris, J. M. Razal, A.I. Minett, Sci. Rep. 6 (2016) 19491.
[33] R. Ding, Y. Chen, P. Chen, R. Wang, J. Wang, Y. Ding, W. Yin, Y. Liu, J. Li, J. Liu, ACS Catal. 11 (2021) 9798–9808.
[34] L. Zhang, Y. Yang, Z. Zhong, F. Yang, H. Su, J. Wang, W. Wang, Electrochim. Acta 544 (2025) 147521.
[35] G. Li, N. Jiang, L. You, M. Wang, L. Zhang, J. Guo, B. Liu, H. Wu, X. Wang, W. Zhu, Appl. Catal. B Environ. 380 (2026) 125805.
[36] Q. Liu, W. Liu, X. Wan, W. Chen, X. Liu, X. Liu, J. Shang, J. Miao, D. Su, X. Sun, J. Shui, Adv. Funct. Mater. 35 (2025) 2507376.
[37] C. Chen, M. Sun, F. Zhang, H. Li, M. Sun, P. Fang, T. Song, W. Chen, J. Dong, B. Rosen, P. Chen, B. Huang, Y. Li, Energy Environ. Sci. 16 (2023) 1685–1696.
[38] M. Kim, K.L. Firestein, J.F.S. Fernando, X. Xu, H. Lim, D.V. Golberg, J. Na, J. Kim, H. Nara, J. Tang, Y. Yamauchi, Chem. Sci. 13 (2022) 10836–10845.
[39] T. Gu, D. Zhang, Y. Yang, C. Peng, D. Xue, C. Zhi, M. Zhu, J. Liu, Adv. Funct. Mater. 33 (2022) 2212299.
[40] K. Ding, J. Hu, L. Zhao, W. Jin, H. Yu, Y. Liu, Z. Wu, S. Cai, Y. Yang, G. Zou, H. Hou, X. Ji, Nano Energy 121 (2024) 109270.
[41] N. Wang, R. Mei, L. Chen, T. Yang, Z. Chen, X. Lin, Q. Liu, Small 20 (2024) 2400327.
[42] Y. Yang, Y. Xiao, L. Zhang, H.T. Wang, K.H. Chen, W.X. Lin, N. Jin, C. Sun, Y.C. Shao, J.L. Chen, J. Qian, L. Han, Appl. Catal. B Environ. 347 (2024) 123792.
[43] M. Yuan, Y. Liu, Y. Du, Z. Xiao, H. Li, K. Liu, L. Wang, Adv. Funct. Mater. 34 (2024) 2401484.
[44] H. Xu, D. Wang, P. Yang, L. Du, X. Lu, R. Li, L. Liu, J. Zhang, M. An, Appl. Catal. B Environ. 305 (2022) 121040.
[45] T. Yang, B. Ge, X. Liu, Z. Zhang, Y. Chen, Y. Liu, J. Mater. Chem. A 12 (2024) 11669–11680.
[46] C.X. Zhao, J.N. Liu, J. Wang, C.D. Wang, X. Guo, X.Y. Li, X. Chen, L. Song, B.Q. Li, Q. Zhang, Sci. Adv. 8 (2022) eabn5091.
[47] C.X. Zhao, J.N. Liu, B.Q. Li, D. Ren, X. Chen, J. Yu, Q. Zhang, Adv. Funct. Mater. 30 (2020) 2003619.
[48] A.I. Douka, Y. Xu, H. Yang, S. Zaman, Y. Yan, H. Liu, M.A. Salam, B.Y. Xia, Adv. Mater. 32 (2020) 2002170.
[49] C.X. Zhao, J.N. Liu, J. Wang, D. Ren, J. Yu, X. Chen, B.Q. Li, Q. Zhang, Adv. Mater. 33 (2021) 2008606.
[50] L. Li, S. Huang, R. Cao, K. Yuan, C. Lu, B. Huang, X. Tang, T. Hu, X. Zhuang, Y. Chen, Small 18 (2021) 2105387.
[51] X. Ma, M. Liu, Q. Li, X. Xiao, J. Liu, X. Xu, Y. Yin, P. Qiao, L. Zhang, X. Zou, R. Wang, B. Jiang, J. Mater. Chem. A 11 (2023) 16889–16899.
[52] X. Liu, F. Zhao, L. Jiao, T. Fang, Z. Zhao, X. Xiao, D. Li, K. Yi, R. Wang, X. Jia, Small 19 (2023) 2300289.
[53] X. Xie, H. Peng, K. Sun, W. Li, A. Liang, G. Ma, Z. Lei, Y. Xu, Adv. Funct. Mater. 34 (2024) 2316037.
[54] M. Guo, M. Ji, W. Cui, Appl. Surf. Sci. 592 (2022) 153237.
[55] H. Li, Y. Huang, Y. Zhang, X. Wang, F. Hu, J. You, K. Zhu, Carbon 232 (2025) 119818.
[56] D. Duan, J. Huo, J. Chen, B. Chi, Z. Chen, S. Sun, Y. Zhao, H. Zhao, Z. Cui, S. Liao, Small 20 (2024) 2310491.
[57] M. Ma, Z. Pei, Y. Peng, R. Hua, Y. Ma, W. Wang, X. Xu, X. Zhang, H. Zheng, J. Mater. Chem. A 13 (2025) 7529–7538.
[58] Y. Qi, W. Shan, H. Yu, J. Cui, Z. Lou, X. Feng, Y. Xiong, Chem. Eng. J. 510 (2025) 161543.
[59] C. Lv, B. Li, Y. Ren, G. Zhang, Z. Lu, L. Li, X. Zhang, X. Yang, X. Yu, Chem. Eng. J. 495 (2024) 153670.
[60] K. Tuo, J. Li, Y. Li, C. Liang, C. Shao, W. Hou, Z. Li, S. Pu, C. Deng, Mater. Horiz. 11 (2024) 3364–3374.
[61] B. Liu, P. Guo, Y. Dai, B. Liu, Z. Zhang, J. Cai, Y. Xia, Q. Pan, L. Shen, Y. Zhang, L. Zhao, Z. Wang, Chem. Eng. J. 507 (2025) 160174.
[62] Z. Gao, H. Wang, J. Zhu, Y. Cao, Q. Zhu, C. Wang, Chem. Eng. J. 506 (2025) 159831.
[63] E. Zhang, T. Wang, K. Yu, J. Liu, W. Chen, A. Li, H. Rong, R. Lin, S. Ji, X. Zheng, Y. Wang, L. Zheng, C. Chen, D. Wang, J. Zhang, Y. Li, J. Am. Chem. Soc. 141 (2019) 16569–16573.
[64] H. Zhou, T. Yang, Z. Kou, L. Shen, Y. Zhao, Z. Wang, X. Wang, Z. Yang, J. Du, J. Xu, M. Chen, L. Tian, W. Guo, Q. Wang, H. Lv, W. Chen, X. Hong, J. Luo, D. He, Y. Wu, Angew. Chem. Int. Ed. 59 (2020) 20465–20469.